LANGMUIR

pubs.acs.org/Langmuir Article

Stabilization and Surface Functionalization of Palladium Disulfide Nanoparticles with Acetylene Derivatives

Xingjian Song, Qiming Liu, Bingzhe Yu, Davida Dubois, and Shaowei Chen*

Cite This: *Langmuir* 2024, 40, 22394−22400 Read Online

ACCESS | Metrics & More | Article Recommendations | Supporting Information

ABSTRACT: Metal chalcogenide nanoparticles have been attracting extensive attention in diverse fields. Traditionally these nanoparticles are stabilized by organic ligands such as thiols and amines involving nonconjugated core-ligand interfacial interactions. In the present study, a facile wet-chemistry method is described for the synthesis of palladium disulfide (PdS_2) nanoparticles capped with acetylene derivatives. Spectroscopic and electrochemical measurements suggest that conjugated Pd−C≡ linkages are formed at the core-ligand interface and facilitate electronic coupling and hence manipulation of the nanoparticle optical and electronic properties. The unique interfacial linkages also allow further functionalization of the nanoparticles by metathesis reaction with olefin derivatives, as manifested in the reaction with vinylferrocene. This research opens new avenues for the structural engineering and functionalization of metal chalcogenide nanoparticles.

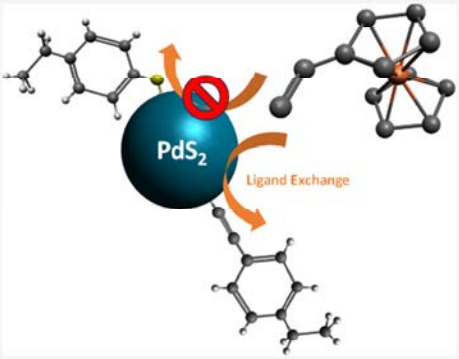

INTRODUCTION

Metal chalcogenide nanoparticles have emerged as a unique family of functional nanomaterials thanks to their distinctive optical and electronic characteristics that find diverse applications in, for instance, photocatalysis, electrochemistry, and biomedicine,[1−5] as compared to their metal counterparts.[6−8] Traditionally, metal chalcogenide nanoparticles are synthesized via hydrothermal, solvothermal, or sol−gel methods and stabilized by organic ligands like thiols, carboxylic acids, amines, etc., leading to manipulation of the nanoparticle hydrophilicity, dipole moments and catalytic performance.[9,10] In these earlier studies, the ligands are primarily involved in nonconjugated interfacial bonding interactions with the inorganic cores, which significantly impedes electronic coupling across the core-ligand interface.[11,12] Such issues can be mitigated when acetylene derivatives are exploited as capping ligands because the resulting conjugated interfacial contact may lead to delocalized hybridization of the metal d electrons and acetylene π electrons.[13−16] In fact, this has been demonstrated with acetylene-capped platinum chalcogenide and ruthenium chalcogenide nanoparticles,[16] which feature metal-acetylene (M−C≡) interfacial linkages and hence effective charge transfer from the metal dichalcogenide core to the acetylene moiety, as opposed to the thiol-capped counterparts. Such electronic hybridization can be exploited for the deliberate regulation of the nanoparticle optical/electronic characterisics and hence their photocatalytic/electrocatalytic applications.[15,16]

One question arises. Is there any feasible way to chemically decorate the nanoparticles with multiple functional moieties? One effective strategy is ligand place exchange reactions.[17] In fact, for acetylene-capped metal nanoparticles, the conjugated M−C≡ interfacial linkages can be exploited for metathesis reactions with vinyl and acetylene derivatives, such that multiple functional moieties can be concurrently incorporated onto the nanoparticle surface.[18] Yet it remains largely explored if such chemistry is extendable to semiconductor nanoparticles, such as metal dichalcogenides, which also entail M−C≡ conjugated linkages at the interface. In a previous study with mercapto-capped gold nanoparticles,[19] the rate and extent of exchange reactions with another mercapto ligands were found to improve with increasingly positively charged gold cores, due to increasing lability of the more ionic Au−S interfacial bonds. Since the metal atoms in metal dichalcogenides are in ionic form, will the resulting M−C≡ interfacial linkages facilitate ligand exchange as well, as compared to the metallic counterparts? This is the major reason for the present work.

Herein, for the first time ever, we successfully prepared palladium disulfide (PdS_2) nanoparticles protected by acetylene derivatives by using a facile wet chemistry procedure. Experimentally, palladium(II) salts and 4-ethylphenylacetlyene (EPA) were first dispersed and mixed in dimethyl sulfoxide (DMSO), into which was added an equimolar amount of sodium sulfide to produce EPA-capped PdS_2 nanoparticles.

Received: August 15, 2024
Revised: September 18, 2024
Accepted: October 4, 2024
Published: October 9, 2024

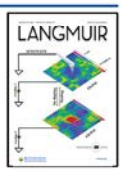

https://doi.org/10.1021/acs.langmuir.4c03199
Langmuir 2024, 40, 22394−22400

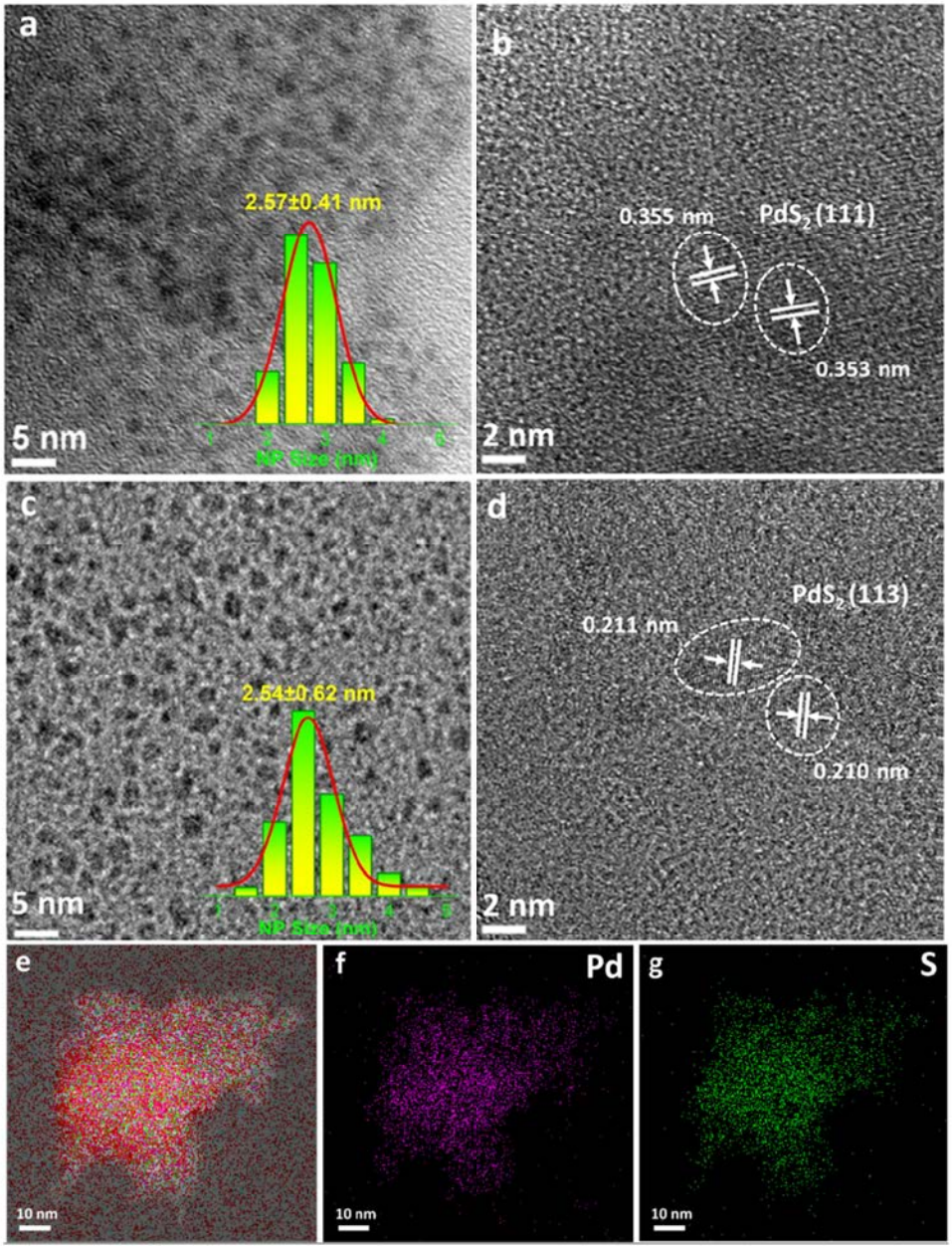

Figure 1. Representative TEM images of (a, b) PdS_2-EPA and (c, d) PdS_2-EPT nanoparticles. The corresponding core size histograms are depicted in the insets to panel (a, c). EDS-based elemental mapping analysis of PdS_2-EPA: (e) overlap, (f) Pd, and (g) S. In panel (e), red is C, blue is O, purple is Pd and green is S.

PdS_2 nanoparticles with 4-ethylphenylthiol (EPT) as capping ligands were synthesized in the same manner as a control. The former entailed the formation of conjugated Pd−C≡ interfacial bonds, whereas nonconjugated Pd−S interfacial linkages were found in the latter. Despite a similar average core size, the two nanoparticles exhibited clearly different optical and electronic properties. In addition, the PdS_2-EPA nanoparticles could be further chemically decorated by metathesis reactions with vinyl directives such as vinylferrocene (vFc), as demonstrated in electrochemical measurements where nanoparticle-mediated intervalence charge transfer (IVCT) was observed due to the particle-bound ferrocenyl moieties.[13] This paves the way for more deliberate engineering of the nanoparticle structure and property.

EXPERIMENTAL SECTION

Reagents. Sodium acetate (NaAc, 99%, Matheson Coleman & Bell), sodium sulfide nonahydrate ($Na_2S{\cdot}9H_2O$, ≥99.99%, Sigma-Aldrich), palladium(II) acetylacetonate ($Pd(acac)_2$, 99%, Sigma-Aldrich), 4-ethylphenylthiol (EPT, >97%, TCI America), 4-ethylphenylacetylene (EPA, 97%, Acros), vinylferrocene (vFc, 99%, Strem Chemicals), tetrabutylammonium hexafluorophosphate ($TBAPF_6$, 98%, Sigma-Aldrich), and solvents were obtained from typical commercial vendors and used as received. Deionized Water was provided with a Barnstead Nanopure water system (resistivity 18.3 MΩ cm).

Sample Preparation. PdS_2-EPA nanoparticles were synthesized by adopting a procedure suggested by ChatGPT with some modifications. In brief, 0.1 mmol of $Pd(acac)_2$ was dispersed in 10 mL of dimethyl sulfoxide (DMSO) in a 100 mL round-bottom flask forming a light-yellow solution. Into this was added 100 μL of EPA

https://doi.org/10.1021/acs.langmuir.4c03199
Langmuir 2024, 40, 22394−22400

ligands and the solution was heated in an oil bath at 80 °C for 1 h under magnetic stirring, followed by the slow addition of 0.1 mmol of $Na_2S{\cdot}9H_2O$ in 10 mL of DMSO, where the solution color was found to change to dark brown, signifying the production of PdS_2 nanoparticles. Fifteen mL of CH_2Cl_2 and 50 mL of H_2O were then added into the reaction vessel, where the nanoparticles were found only in the CH_2Cl_2 layer, whereas the H_2O/DMSO layer was clear (Figure S1a,b). The CH_2Cl_2 phase was saved with a separatory funnel and washed several times with water until the aqueous phase was totally clear. Rotary evaporation was performed to remove the solvents, and the obtained solids (PdS_2-EPA) were washed with a large amount of methanol. The PdS_2-EPT sample was prepared in the same fashion but by using an equivalent amount of EPT in place of EPA, featuring an orange/brown color in CH_2Cl_2 (Figure S1c). Notably, both PdS_2-EPA and PdS_2-EPT nanoparticles were easily dispersible in a variety of nonpolar solvents, e.g., CH_2Cl_2, THF, and toluene, in sharp contrast to the "bare" nanoparticles prepared without the addition of either EPA or EPT ligands (Figure S2). The nanoparticles also remained stable under ambient conditions, suggesting sufficient protection by the respective ligands (Figure S3).

EPA-capped metallic Pd (Pd-EPA) nanoparticles were prepared as another control by a thermolytic reduction procedure in ethylene glycol, as detailed previously.[20] Experimentally, $Pd(acac)_2$ (0.3 mmol) and NaAc (1 mmol) were dispersed in ethylene glycol (100 mL) under sonication forming a light-yellow solution in a 250 mL round-bottom flask, which was then heated to 200 °C in an oil bath under vigorous stirring and refluxed for 15 min. The solution color was observed to gradually change to dark brown, signifying the generation of "bare" Pd colloidal particles. When the solution temperature went down to ca. 80 °C, 30 mL of toluene containing 200 μL of EPA ligands was added into the solution under magnetic stirring for 1 h. An excessive amount of water was then added to induce phase segregation, where the particles were collected from the toluene phase whereas the ethylene glycol phase was clear (Figure S4). Rotary evaporation was then performed to remove the solvents and the obtained solids were washed extensively with methanol, affording Pd-EPA nanoparticles.

Ligand-Exchange Reactions. The nanoparticles obtained above were further functionalized by ligand exchange reactions. In brief, PdS_2-EPA or Pd-EPA nanoparticles was dispersed in 10 mL of CH_2Cl_2, into which was added a calculated amount of vFc (Fe/Pd atomic ratio 3:1) under vigorous stirring at room temperature for 3 days. Rotary evaporation was then performed to remove solvents, and the solids were purified by rinsing with methanol. The resulting nanoparticles were denoted as PdS_2-EPA_{Fc} and Pd-EPA_{Fc}, respectively.

Characterizations. Proton nuclear magnetic resonance (^{1}H NMR) measurements of the nanoparticle samples were conducted in CD_2Cl_2 with a Bruker Avance III HD 800 MHz spectrometer. Infrared spectra were obtained with a PerkinElmer Spectrum One Fourier transform infrared spectrometer (FTIR) with the samples prepared by dropcasting the nanoparticle solutions in CH_2Cl_2 onto a NaCl plate. Raman spectra were acquired with a Horiba Jobin Yvon LabRAM ARAMIS automated scanning confocal Raman microscope (excitation wavelength 532 nm). Ultraviolet−visible (UV−vis) absorption spectra were collected with a PerkinElmer Lambda 35 UV−vis spectrometer, and a PTI fluorospectrometer was used to produce the photoluminescence (PL) profiles. X-ray photoelectron spectroscopy (XPS) analysis was completed with a Thermo Fisher K-alpha system. Transmission electron microscopy (TEM) studies were performed with a Tecnai G2 instrument operated at 200 kV.

Electrochemistry. Voltametric measurements were conducted with a CHI 440 electrochemical workstation. The working electrode was a polycrystalline gold disk electrode (sealed in a glass tubing, surface area 0.9 mm^2), along with a Ag/AgCl quasi-reference and a Pt coil counter electrode. The gold electrode was polished with 0.05 μm alumina slurries and rinsed with 0.1 M $HClO_4$, ethanol and deionized water before electrochemical measurements.

RESULTS AND DISCUSSION

TEM measurements were first carried out to characterize the nanoparticle structures. From Figure 1a,c, one can see that both PdS_2-EPA and PdS_2-EPT nanoparticles displayed good dispersion without obvious aggregation, indicating sufficient protection of the nanoparticles by the respective ligands (Figure S3). Statistical analysis from over 100 nanoparticles revealed that the nanoparticle diameters were mostly between 2 and 3 nm, with an average of 2.57 ± 0.41 nm for PdS_2-EPA and 2.54 ± 0.62 nm for PdS_2-EPT, as evidenced in the respective core size histogram (insets to Figure 1a,c). Furthermore, clearly defined lattice fringes can be observed in high-resolution TEM measurements of both samples (Figure 1b,d), and an interplanar spacing of ca. 0.355 nm can be estimated for PdS_2-EPA (Figure S5a) and 0.211 nm for PdS_2-EPT (Figure S5b), which can be ascribed to the (111) and (113) planes of orthorhombic PdS_2 (mp-13682), respectively. Indeed, in Raman measurements, both nanoparticles can be found to exhibit a broad vibrational band centered at ca. 350 cm^{-1}, consistent with the characteristic vibrations of Pd−S (Figure S6a).[21] Elemental mapping analysis based on energy-dispersive X-ray spectroscopy (EDS) shows that the Pd and S elements were indeed distributed rather evenly across the samples (Figure 1e−g).

Consistent results were obtained from ^{1}H NMR measurements. Figure S6b shows the ^{1}H NMR spectra, where the spectral features of the methyl (1.16−1.25 ppm), methylene (2.48−2.68 ppm) and phenyl protons (6.66−7.17 ppm) were significantly broadened for both samples, as compared to the respective monomeric ligands (Table S1), due to a reduced T_2 relaxation time.[22] The lack of sharp features also signifies that the samples were free of excessive ligands.[22] The sample structures were further probed by FTIR spectroscopic measurements. From the FTIR spectra in Figure S6c, it can be seen that all nanoparticles possessed three obvious bands at 2871, 2922, and 2962 cm^{-1}, due to the CH_3/CH_2 stretching vibrations of the ethyl group of the EPA and EPT ligands, and multiple vibrations between 3100 and 3000 cm^{-1} arising from the phenyl =C−H.[23,24] Meanwhile, the absence of the terminal H−C≡ vibration (ca. 3300 cm^{-1}) in PdS_2-EPA and Pd-EPA and S−H vibration (ca. 2570 cm^{-1}) in PdS_2-EPT signifies that excessive EPA and EPT ligands were indeed removed from the samples. Concurrently, the C≡C vibration can be seen to red-shift from 2100 cm^{-1} for EPA to 1905 cm^{-1} for PdS_2-EPA, as the Pd−C≡ interfacial linkages facilitated electronic coupling between the ligand π electrons and Pd d electrons.[18]

XPS measurements were then carried out to probe the elemental composition and valency of the samples. The survey spectra are depicted in Figure S7a, where the S 2p, C 1s, Pd 3d and O 1s electrons can be easily resolved in both samples at ca. 162, 284, 336, and 532 eV, respectively. On the basis of the intergrated peak areas, the Pd/S atomic ratio was evaluated at 1:2.03 for PdS_2-EPA and 1:2.31 for PdS_2-EPT (Tables S2 and S3).[25−27] These are in accord with the formation of PdS_2 nanoparticle cores in the samples, as suggested in the TEM measurements presented above. The slightly higher sulfur content in PdS_2-EPT can be attributable to the additional contributions from the EPT ligands.[28]

Figure 2a depicts the high-resolution profiles of the Pd 3d electrons. Both PdS_2-EPA and PdS_2-EPT nanoparticles can be seen to possess one doublet, with the binding energies at

https://doi.org/10.1021/acs.langmuir.4c03199
Langmuir 2024, 40, 22394−22400

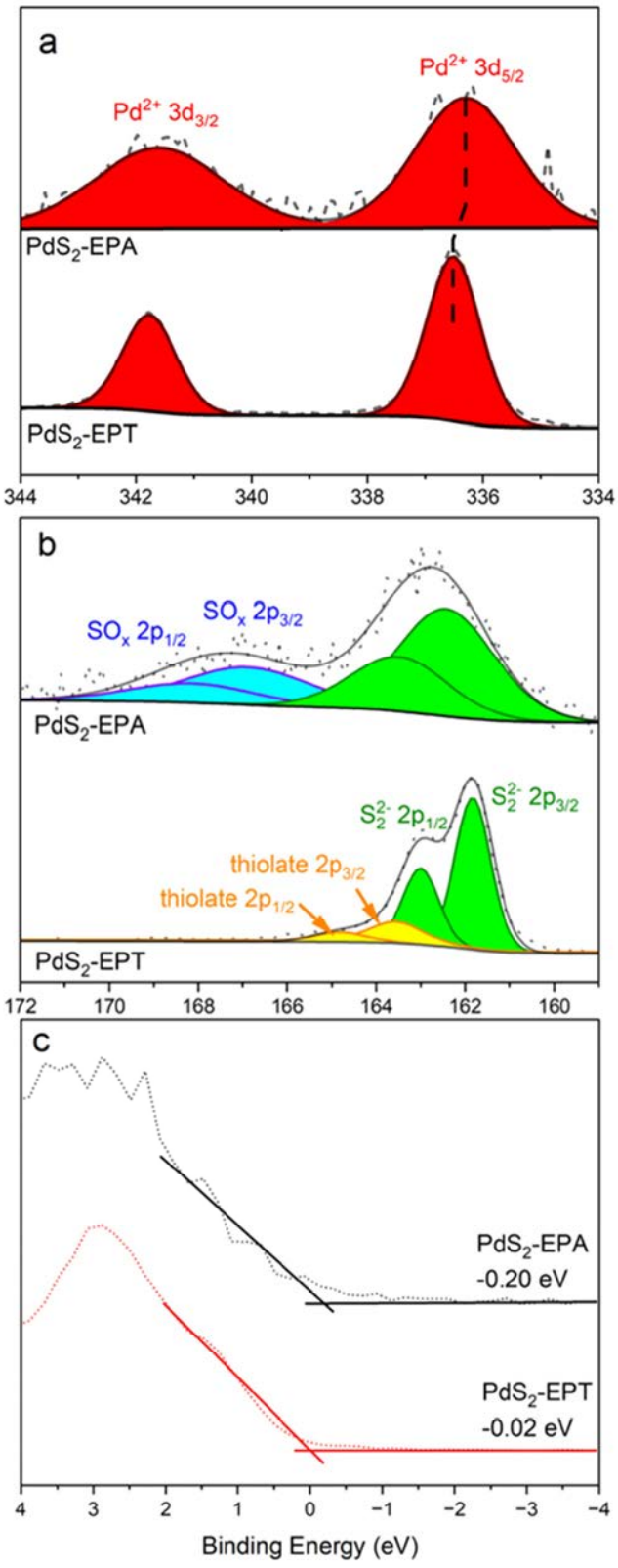

Figure 2. High-resolution scans of the (a) Pd 3d and (b) S 2p electrons of PdS_2-EPA and PdS_2-EPT. Dotted curves are experimental data and colored peaks are deconvolution fits. (c) VBM spectra of PdS_2-EPA and PdS_2-EPT.

336.29/342.60 and 336.50/341.77 eV, respectively, that can be ascribed to the $3d_{5/2}/3d_{3/2}$ electrons of Pd^{2+}.[28,29] Notably, the binding energies were over 0.2 eV lower for the former than for the latter, suggesting electron-enriched Pd in PdS_2-EPA, most likely arising from the generation of Pd−C≡ interfacial linkages and electron transfer from the EPA ligands. One may notice that in the previous study of EPA-capped platinum and ruthenium chalcogenide nanoparticles, the conjugated interfacial bonds facilitated core to ligand electron transfer instead.[16] Such a discrepancy may be ascribed to the unique $[Kr]4d^{10}$ electronic configuration of Pd, in comparison to $[Xe]4f^{14}5d^{9}6s^{1}$ for Pt and $[Kr]4d^{7}5s^{1}$ for Ru, such that it is energetically more favorable for Pd^{2+} to accept electrons to reach the stable $4d^{10}$ configuration.

In addition, one can see that the peak width of PdS_2-EPA was drastically greater than that of PdS_2-EPT. This is likely because of the more complex chemical environments of the Pd centers in the former, consisting of those in the nanoparticle core that were bonded to S only and the surface ones that were bonded to both S and −C≡ (ca. 40% of Pd resided on the surface of PdS_2 nanoparticles of 2.54 nm in diameter, Figure 1), whereas for PdS_2-EPT, the chemical environments were relatively uniform for the surface and interior Pd.

The corresponding S 2p spectra are shown in Figure 2b. Deconvolution of the S 2p spectrum of PdS_2-EPT yields two doublets, with the dominant one at 161.83/162.89 eV for S_2^{2-}, and a small one at 162.5/163.5 eV for thiolate moieties of the EPT ligands.[30] The PdS_2-EPA sample also consisted of two doublets, a major doublet at ca. 162.42/163.48 eV that can be ascribed to the $2p_{3/2}/2p_{1/2}$ electrons of S_2^{2-}, with a minor one at 166.89/168.15 eV for oxidized S, likely arising from partial oxidation of the PdS_2 cores.[16] The fact that the Pd^{2+} (S_2^{2-}) binding energy of PdS_2-EPA showed an obvious red (blue) shift in comparison to those of PdS_2-EPT suggests that the nanoparticle cores were less polar in the former, likely due to the conjugated Pd−C≡ interfacial bonds that facilitated electronic coupling with the π electrons of the EPA ligands.

The C 1s scans further validated the existence of EPA and EPT ligands on the surfaces of the PdS_2 nanoparticles (Figure S7b). Three species can be deconvoluted from the spectrum of PdS_2-EPA at ca. 283.29 eV for sp C (from C≡C), ca. 283.87 eV for sp^2 C (from phenyl C═C) and ca. 284.53 eV for sp^3 C (from the ethyl moiety), in good agreement with the ligand structure of EPA.[16,31] In comparison, only two species can be resolved for the PdS_2-EPT sample, one at ca. 283.79 eV for sp^2 C (from C═C) and the other at ca. 284.33 eV for sp^3 (from the ethyl moiety).[16,30] Notably, from the O 1s spectra in Figure S7c, no peak can be resolved under 530.0 eV, indicating that the nanoparticles contained no metal-O species.[16]

More information about the interfacial charge transfer can be inferred from the valence band maximum (VBM) spectra. As shown in Figure 2c, PdS_2-EPA displayed a VBM of ca. −0.20 eV, in comparison to −0.02 eV for PdS_2-EPT,[16] indicating that the Fermi level shifted further away from the d band for the former than for the latter, which can be ascribed to electron enrichment due to interfacial charge transfer from the EPA ligands to the PdS_2 cores, in consistence with the XPS results presented above.

UV−vis absorption measurements were then performed to probe the optical properties of the nanoparticles. As shown in Figure 3a, a broad absorption peak appeared at ca. 400 nm for PdS_2-EPA, and the peak became drastically prominent for PdS_2-EPT. Furthermore, two sharp absorption bands can be observed at 313 and 334 nm for PdS_2-EPA and 287 and 298 nm for PdS_2-EPT, most likely due to the $\pi-\pi^*$ transitions of

https://doi.org/10.1021/acs.langmuir.4c03199
Langmuir 2024, 40, 22394−22400

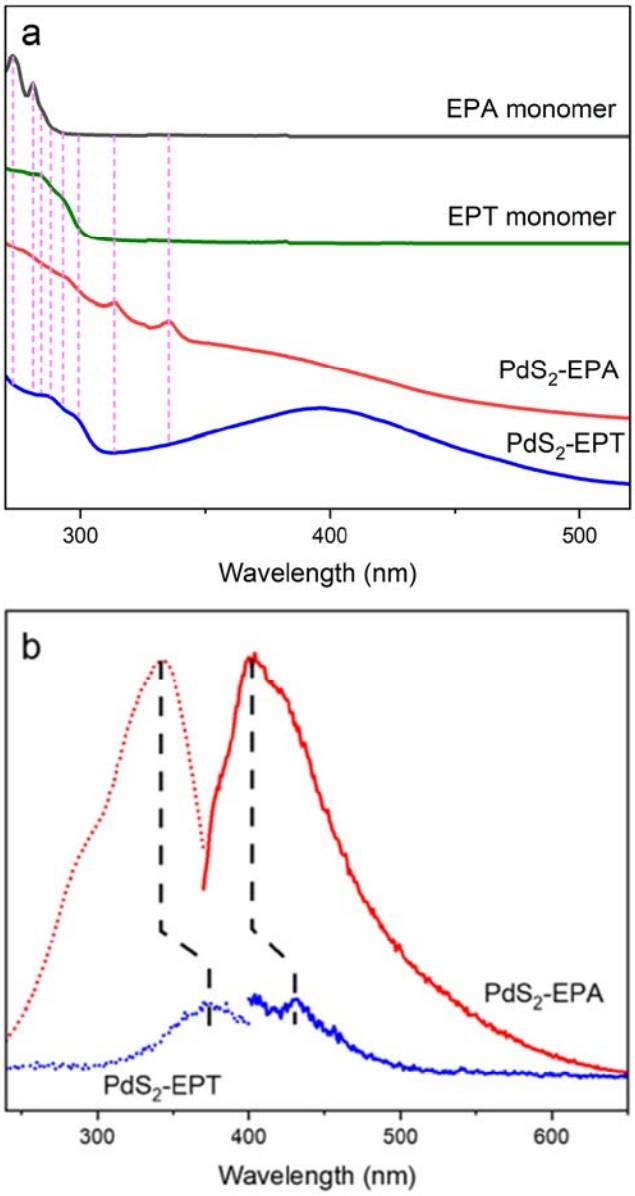

Figure 3. (a) Optical absorption and (b) photoluminescence excitation (dotted curves) and emission spectra (solid curves) of PdS_2-EPA and PdS_2-EPT nanoparticles. The excitation and emission peak positions are 342 and 401 nm for PdS_2-EPA and 374 and 431 nm for PdS_2-EPT.

the phenyl moieties.[32] The fact that the former exhibit a more prominent red-shift than the latter as compared to monomeric EPA (273 and 281 nm) and EPT (283 and 293 nm) further confirmed enhanced electronic coupling between the core and ligands in PdS_2-EPA.

In photoluminescence (PL) measurements (Figure 3b), PdS_2-EPA nanoparticles can be seen to exhibit a well-defined emission peak at 401 nm when excited at 342 nm, due to conjugated core-ligand interfacial linkages that facilitated intraparticle charge delocalization. Therefore. the particle-attached ligands acted comparably to diacetylene moieties.[13] In comparison, with nonconjugated Pd−S interfacial linkages, PdS_2-EPT showed only a weak emission peak at 431 nm at the excitation of 374 nm that can be ascribed to the PdS_2 cores.[33] This further confirms the notion that the PL emission of PdS_2-EPA was primarily due to the particle-bound EPA ligands, rather than the PdS_2 cores (Figure S8).

Significantly, the formation of conjugated Pd−C≡ interfacial bonds in PdS_2-EPA rendered it possible to further functionalize the nanoparticles by metathesis reactions with vinyl/acetylene derivatives (e.g., vFc), in contrast to the PdS_2-EPT counterpart.[18] Figure 4 displays the differential pulse voltammograms (DPV) of the PdS_2-EPA_{Fc} nanoparticles in CH_2Cl_2 containing 0.1 M $TBAPF_6$ supporting electrolyte. In comparison to the featureless profile of PdS_2-EPA (black curves) within the potential range of 0.0 to +1.0 V, the PdS_2-EPA_{Fc} sample exhibited a single pair of voltammetric peaks in the dark featuring a formal potential ($E^{o\prime}$) of +0.568 V (blue curves), due to the redox reactions of the Fc moieties, confirming successful decoration of the nanoparticle surface with the ferrocenyl moieties by metathesis reaction (consistent results were obtained in cyclic voltametric measurements, Figure S9). In sharp contrast, when the experiment was conducted under 365 nm UV photoirradiation, two pairs of voltammetric peaks emerged, and the formal potentials can be found at +0.388 and +0.602 V (red curves), suggesting IVCT of the particle-attached ferrocenyl moieties, and the peak separation ($\Delta E^{o\prime}$) of 214 mV suggests class II IVCT.[4,24,31] This can be ascribed to the electrically insulating PdS_2 cores in the dark that became conducting under UV irradiation, such that the IVCT behaviors were consistent with those with metallic Pd-EPA_{Fc} counterparts ($\Delta E^{o\prime}$ = 242 mV, Figure S10).[4,24,31]

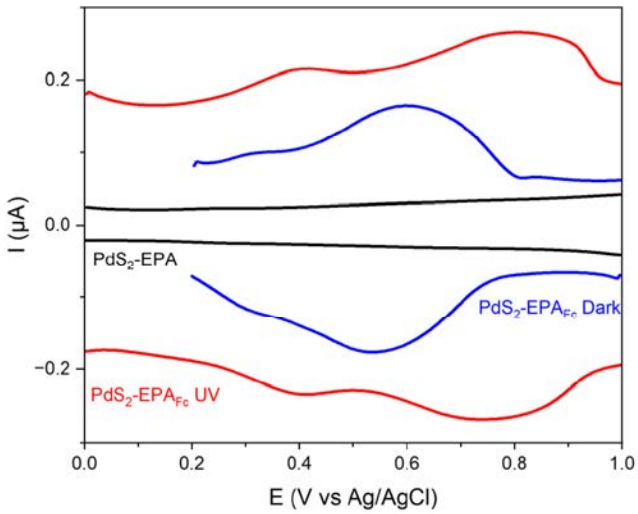

Figure 4. Differential pulse voltammograms of PdS_2-EPA and PdS_2-EPA_{Fc} nanoparticles acquired in the dark and under UV photoirradiation in 0.1 M $TBAPF_6$ containing 10 mg/mL nanoparticles in CH_2Cl_2. Pulse period 0.2 s, pulse width 50 ms, pulse amplitude 50 mV, sample width 16.7 ms, and quiet time 2 s.

The decoration of the nanoparticle surface with the vFc ligands was further supported by the apparent quenching of the PL emission of PdS_2-EPA_{Fc} (Figure S11), likely due to energy/electron transfer to the ferrocenyl moiety, as the absorption profile of vFc exhibits a significant overlap with the PL emission of the PdS_2-EPA nanoparticle and the ferrocenyl moieties are attached via conjugated interfacial linkages onto the nanoparticle surface.[34] Furthermore, in comparison to metallic Pd-EPA nanoparticles, the metathesis reaction was found to be markedly enhanced with PdS_2-EPA. In fact, after

https://doi.org/10.1021/acs.langmuir.4c03199
Langmuir 2024, 40, 22394−22400

72 h exchange reaction, XPS measurements showed that the Fe/Pd atomic ratio was only 0.021 with metallic Pd-EPA nanoparticles, and increased significantly to 0.448 with PdS_2-EPA. The enhanced efficiency can be ascribed to the Pd^{2+} centers in the latter that rendered the Pd−C≡ interfacial bonds more labile (ionic) for metathesis reactions.[19]

CONCLUSIONS

A solution chemistry route was described for the facile preparation of acetylene-stabilized palladium disulfide nanoparticles. The forming of conjugated Pd−C≡ interfacial linkages facilitated effective charge transfer from the organic ligands to the inorganic cores, resulting in ready manipulation of the nanoparticle optical and electronic properties. Furthermore, the nanoparticles could undergo more complicated surface functionalization by metathesis reactions, as manifested in the exchange reaction with vinylferrocene where IVCT was observed with the nanoparticle-bound ferrocene moieties under UV photoirradiation. Notably, the metathesis reaction efficacy was markedly enhanced as compared to metallic Pd nanoparticles, due to the more ionic and hence more labile interfacial linkages. These results highlight the significance of nanoparticle surface chemistry in their surface functionalization and properties.

ASSOCIATED CONTENT

Supporting Information

The Supporting Information is available free of charge at https://pubs.acs.org/doi/10.1021/acs.langmuir.4c03199.

Additional experimental data; photographs of nanoparticle synthesis; live profiles of TEM lattice fringes; additional XPS, UV−vis, and PL spectra; additional electrochemical data; tables of NMR peaks and XPS fittings (PDF)

AUTHOR INFORMATION

Corresponding Author

Shaowei Chen − *Department of Chemistry and Biochemistry, University of California, Santa Cruz, California 95064, United States;* orcid.org/0000-0002-3668-8551; Email: shaowei@ucsc.edu

Authors

Xingjian Song − *Department of Chemistry and Biochemistry, University of California, Santa Cruz, California 95064, United States*

Qiming Liu − *Department of Chemistry and Biochemistry, University of California, Santa Cruz, California 95064, United States*

Bingzhe Yu − *Department of Chemistry and Biochemistry, University of California, Santa Cruz, California 95064, United States*

Davida Dubois − *Department of Chemistry and Biochemistry, University of California, Santa Cruz, California 95064, United States;* orcid.org/0000-0002-2612-3717

Complete contact information is available at: https://pubs.acs.org/10.1021/acs.langmuir.4c03199

Author Contributions

The manuscript was written through contributions of all authors. All authors have given approval to the final version of the manuscript.

Notes

The authors declare no competing financial interest.

ACKNOWLEDGMENTS

The authors thank the National Science Foundation for financial support of the work through grants CHE-1900235 and CHE-2003685. TEM, XPS, and Raman data were acquired at the Molecular Foundry and National Center for Electron Microscopy, Lawrence Berkeley National Laboratory, which is supported by the Office of Science, Office of Basic Energy Sciences of the U.S. Department of Energy under Contract No. DE-AC02- 475 05CH11231. Dr. L. Klivansky's assistance in FTIR measurements is also greatly appreciated.

REFERENCES

(1) Kershaw, S. V.; Susha, A. S.; Rogach, A. L. Narrow bandgap colloidal metal chalcogenide quantum dots: synthetic methods, heterostructures, assemblies, electronic and infrared optical properties. *Chem. Soc. Rev.* **2013**, *42* (7), 3033−3087.

(2) Zhang, Y.; Zhou, Q.; Zhu, J.; Yan, Q.; Dou, S. X.; Sun, W. Nanostructured Metal Chalcogenides for Energy Storage and Electrocatalysis. *Adv. Funct. Mater.* **2017**, *27* (35), No. 1702317.

(3) Zhou, J.; Lin, J.; Huang, X.; Zhou, Y.; Chen, Y.; Xia, J.; Wang, H.; Xie, Y.; Yu, H.; Lei, J.; Wu, D.; Liu, F.; Fu, Q.; Zeng, Q.; Hsu, C.-H.; Yang, C.; Lu, Y.; Yu, T.; Shen, Z.; Lin, H.; Yakobson, B. I.; Liu, Q.; Suenaga, K.; Liu, G.; Liu, Z. A library of atomically thin metal chalcogenides. *Nature* **2018**, *556* (7701), 355−359.

(4) Wang, X.; Long, H.; Qarony, W.; Tang, C. Y.; Yuan, H.; Tsang, Y. H. Fabrication of luminescent PtS2 quantum dots. *J. Lumin.* **2019**, *211*, 227−232.

(5) Chen, H.; Ran, M.-Y.; Wei, W.-B.; Wu, X.-T.; Lin, H.; Zhu, Q.-L. A comprehensive review on metal chalcogenides with three-dimensional frameworks for infrared nonlinear optical applications. *Coord. Chem. Rev.* **2022**, *470*, No. 214706.

(6) Cordones, A. A.; Scheele, M.; Alivisatos, A. P.; Leone, S. R. Probing the interaction of single nanocrystals with inorganic capping ligands: time-resolved fluorescence from CdSe-CdS quantum dots capped with chalcogenidometalates. *J. Am. Chem. Soc.* **2012**, *134* (44), 18366−18373.

(7) Cao, X.; Ding, C.; Zhang, C.; Gu, W.; Yan, Y.; Shi, X.; Xian, Y. Transition metal dichalcogenide quantum dots: synthesis, photoluminescence and biological applications. *J. Mater. Chem. B* **2018**, *6* (48), 8011−8036.

(8) Giansante, C. Library Design of Ligands at the Surface of Colloidal Nanocrystals. *Acc. Chem. Res.* **2020**, *53* (8), 1458−1467.

(9) Bertolotti, F.; Dirin, D. N.; Ibanez, M.; Krumeich, F.; Cervellino, A.; Frison, R.; Voznyy, O.; Sargent, E. H.; Kovalenko, M. V.; Guagliardi, A.; Masciocchi, N. Crystal symmetry breaking and vacancies in colloidal lead chalcogenide quantum dots. *Nat. Mater.* **2016**, *15* (9), 987−994.

(10) Mourdikoudis, S.; Menelaou, M.; Fiuza-Maneiro, N.; Zheng, G.; Wei, S.; Perez-Juste, J.; Polavarapu, L.; Sofer, Z. Oleic acid/oleylamine ligand pair: a versatile combination in the synthesis of colloidal nanoparticles. *Nanoscale Horiz.* **2022**, *7* (9), 941−1015.

(11) Yazdani, N.; Volk, S.; Yarema, O.; Yarema, M.; Wood, V. Size, Ligand, and Defect-Dependent Electron−Phonon Coupling in Chalcogenide and Perovskite Nanocrystals and Its Impact on Luminescence Line Widths. *ACS Photonics* **2020**, *7* (5), 1088−1095.

(12) Kennehan, E. R.; Munson, K. T.; Grieco, C.; Doucette, G. S.; Marshall, A. R.; Beard, M. C.; Asbury, J. B. Influence of Ligand Structure on Excited State Surface Chemistry of Lead Sulfide Quantum Dots. *J. Am. Chem. Soc.* **2021**, *143* (34), 13824−13834.

(13) Kang, X.; Zuckerman, N. B.; Konopelski, J. P.; Chen, S. Alkyne-functionalized ruthenium nanoparticles: ruthenium-vinylidene bonds at the metal-ligand interface. *J. Am. Chem. Soc.* **2012**, *134* (3), 1412−1415.

(14) Peng, Y.; Hirata, E. Y.; Pan, W.; Chen, L.; Lu, J. E.; Chen, S. Intraparticle charge delocalization through conjugated metal-ligand interfacial bonds: Effects of metal d electrons. *Chin. J. Chem. Phys.* **2018**, *31* (4), 433−438.
(15) Liu, Q.; Peng, Y.; Masood, Z.; DuBois, D.; Tressel, J.; Nichols, F.; Ashby, P.; Mercado, R.; Assafa, T.; Pan, D.; Kuo, H.-L.; Lu, J. Q.; Bridges, F.; Millhauser, G. L.; Ge, Q. F.; Chen, S. Stable Cuprous Hydroxide Nanostructures by Organic Ligand Functionalization. *Adv. Mater.* **2023**, *35* (8), No. 2208665.
(16) Liu, Q.; Song, X.; DuBois, D.; Yu, B.; Bhuller, A.; Flannery, G.; Hawley, M.; Bridges, F.; Chen, S. Alkyne-Functionalized Platinum Chalcogenide (S, Se) Nanoparticles. *Inorg. Chem.* **2024**, *63* (2), 1046−1053.
(17) Hicks, J. F.; Zamborini, F. P.; Osisek, A. J.; Murray, R. W. The Dynamics of Electron Self-Exchange between Nanoparticles. *J. Am. Chem. Soc.* **2001**, *123* (29), 7048−7053.
(18) Hu, P.; Chen, L.; Kang, X.; Chen, S. Surface Functionalization of Metal Nanoparticles by Conjugated Metal-Ligand Interfacial Bonds: Impacts on Intraparticle Charge Transfer. *Acc. Chem. Res.* **2016**, *49* (10), 2251−2260.
(19) Song, Y.; Murray, R. W. Dynamics and extent of ligand exchange depend on electronic charge of metal nanoparticles. *J. Am. Chem. Soc.* **2002**, *124* (24), 7096−7102.
(20) He, G. Q.; S, Y.; Kang, X. W.; Chen, S. W. Alkyne-functionalized palladium nanoparticles: Synthesis, characterization, and electrocatalytic activity in ethylene glycol oxidation. *Electrochim. Acta* **2013**, *94*, 98−103.
(21) Zhang, X.; Su, G.; Lu, J.; Yang, W.; Zhuang, W.; Han, K.; Wang, X.; Wan, Y.; Yu, X.; Yang, P. Centimeter-Scale Few-Layer PdS(2): Fabrication and Physical Properties. *ACS Appl. Mater. Interfaces* **2021**, *13* (36), 43063−43074.
(22) Terrill, R. H.; Postlethwaite, T. A.; Chen, C. H.; Poon, C. D.; Terzis, A.; Chen, A.; Hutchison, J. E.; Clark, M. R.; Wignall, G. Monolayers in three dimensions: NMR, SAXS, thermal, and electron hopping studies of alkanethiol stabilized gold clusters. *J. Am. Chem. Soc.* **1995**, *117* (50), 12537−12548.
(23) Lhuillier, E.; Pedetti, S.; Ithurria, S.; Nadal, B.; Heuclin, H.; Dubertret, B. Two-dimensional colloidal metal chalcogenides semiconductors: synthesis, spectroscopy, and applications. *Acc. Chem. Res.* **2015**, *48* (1), 22−30.
(24) Peng, Y.; Lu, J. E.; Deming, C. P.; Chen, L.; Wang, N.; Hirata, E. Y.; Chen, S. Photo-Gated Intervalence Charge Transfer of Ethynylferrocene Functionalized Titanium Dioxide Nanoparticles. *Electrochim. Acta* **2016**, *211*, 704−710.
(25) Li, Y.; Yu, S.; Doronkin, D. E.; Wei, S.; Dan, M.; Wu, F.; Ye, L.; Grunwaldt, J.-D.; Zhou, Y. Highly dispersed PdS preferably anchored on In_2S_3 of MnS/In_2S_3 composite for effective and stable hydrogen production from H_2S. *J. Catal.* **2019**, *373*, 48−57.
(26) Chen, E.; Xu, W.; Chen, J.; Warner, J. H. 2D layered noble metal dichalcogenides (Pt, Pd, Se, S) for electronics and energy applications. *Mater. Today Adv.* **2020**, *7*, No. 100076.
(27) Liu, Q.; Peng, Y.; Li, Q.; He, T.; Morris, D.; Nichols, F.; Mercado, R.; Zhang, P.; Chen, S. Atomic Dispersion and Surface Enrichment of Palladium in Nitrogen-Doped Porous Carbon Cages Lead to High-Performance Electrocatalytic Reduction of Oxygen. *ACS Appl. Mater. Interfaces* **2020**, *12* (15), 17641−17650.
(28) Romanchenko, A. S.; Mikhlin, Y. L. An XPS study of products formed on pyrite and pyrrhotine by reacting with palladium(II) chloride solutions. *J. Struct. Chem.* **2015**, *56* (3), 531−537.
(29) Hyland, M. M.; Bancroft, G. M. Palladium sorption and reduction on sulphide mineral surfaces: An XPS and AES study. *Geochim. Cosmochim. Acta* **1990**, *54*, 117−130.
(30) Castner, D. G.; H, K.; Grainger, D. W. X-ray Photoelectron Spectroscopy Sulfur 2p Study of Organic Thiol and Disulfide Binding Interactions with Gold Surfaces. *Langmuir* **1996**, *12* (21), 5083−5086.
(31) Peng, Y.; Liu, Q.; Lu, B.; He, T.; Nichols, F.; Hu, X.; Huang, T.; Huang, G.; Guzman, L.; Ping, Y.; Chen, S. Organically Capped Iridium Nanoparticles as High-Performance Bifunctional Electrocatalysts for Full Water Splitting in Both Acidic and Alkaline Media: Impacts of Metal−Ligand Interfacial Interactions. *ACS Catal.* **2021**, *11* (3), 1179−1188.
(32) Ma, Y.; Hu, C.; Guo, H.; Fan, L.; Yang, S.; Sun, W.-H. Structure effect on transition mechanism of UV−visible absorption spectrum in polyimides: A density functional theory study. *Polymer* **2018**, *148*, 356−369.
(33) Wang, X.; Qarony, W.; Cheng, P. K.; Ismail, M.; Tsang, Y. H. Photoluminescence of PdS_2 and $PdSe_2$ quantum dots. *RSC Adv.* **2019**, *9* (65), 38077−38084.
(34) Dorokhin, D.; Tomczak, N.; Velders, A. H.; Reinhoudt, D. N.; Vancso, G. J. Photoluminescence Quenching of CdSe/ZnS Quantum Dots by Molecular Ferrocene and Ferrocenyl Thiol Ligands. *J. Phys. Chem. C* **2009**, *113* (43), 18676−18680.

https://doi.org/10.1021/acs.langmuir.4c03199
Langmuir 2024, 40, 22394−22400